

Article

Electrochemical–Thermal Modeling of Lithium-Ion Batteries: An Analysis of Thermal Runaway with Observation on Aging Effects

Milad Tulabi  and Roberto Bubbico * 

Department of Chemical Materials and Environmental Engineering, “Sapienza” Rome University, Via Eudossiana 18, 00184 Rome, Italy; milad.tulabi@uniroma1.it

* Correspondence: roberto.bubbico@uniroma1.it

Abstract: The increasing demand for energy storage solutions, particularly in electric vehicles and renewable energy systems, has intensified research on lithium-ion (Li-ion) battery safety and performance. A critical challenge is thermal runaway (TR), a highly exothermic sequence of reactions triggered by mechanical, electrical, or thermal abuse, which can lead to catastrophic failures. While most TR models focus on fresh cells, aging significantly impacts battery behavior and safety. This study develops an electrochemical–thermal coupled model that incorporates aging effects to better predict thermal behavior and TR initiation in cylindrical Li-ion batteries. The model is validated against experimental data for fresh NMC and aged NCA cells, and statistical analysis is conducted to identify key factors influencing TR ($p < 0.05$). A full factorial design evaluates the effects of internal resistance (10, 20, 30, and 40 mΩ), capacity (1, 2, 3, and 5 Ah), and current rate (1C, 3C, 6C, and 8C) on temperature evolution. Additionally, a machine learning algorithm (logistic regression) is employed to identify an internal resistance threshold, beyond which thermal runaway (TR) becomes highly probable, and to predict TR probability based on key battery parameters. The model achieved a high prediction accuracy of 95% on the test dataset. Results indicate that aging affects thermal stability in complex ways. The increased internal resistance exacerbates heating rates, while capacity fade reduces stored energy, mitigating TR risk. These findings provide a validated framework for enhancing battery thermal management and predictive safety mechanisms, which contributed to the development of safer, more reliable Li-ion energy storage systems.



Academic Editor: Sylvain Franger

Received: 17 March 2025

Revised: 25 April 2025

Accepted: 27 April 2025

Published: 2 May 2025

Citation: Tulabi, M.; Bubbico, R. Electrochemical–Thermal Modeling of Lithium-Ion Batteries: An Analysis of Thermal Runaway with Observation on Aging Effects. *Batteries* **2025**, *11*, 178. <https://doi.org/10.3390/batteries11050178>

Copyright: © 2025 by the authors. Licensee MDPI, Basel, Switzerland. This article is an open access article distributed under the terms and conditions of the Creative Commons Attribution (CC BY) license (<https://creativecommons.org/licenses/by/4.0/>).

Keywords: thermal runaway; Li-ion battery; modeling; aging; battery safety

1. Introduction

The energy sector’s reliance on fossil fuels contributes significantly to global greenhouse gas emissions and air pollution annually [1]. Rising demand, resource depletion, and geopolitical instability also induce a shift toward low-carbon energy sources such as wind and solar power. To balance the variability of renewable energy, efficient energy storage solutions like secondary (rechargeable) batteries and supercapacitors are critical. The ongoing transition to fully electric and hybrid vehicles to reduce transportation-related emissions already represents an example of this paradigm shift.

Li-ion batteries have become a cornerstone of low-carbon energy applications due to their high energy density and compact design, particularly in electric vehicles (EVs) and portable devices. However, their safety has gained attention due to the risks of catastrophic failures like thermal runaway [2–5]. Thermal runaway (TR) occurs when an uncontrollable

rise in temperature leads to strongly exothermic side reactions, such as those associated with the decomposition of the solid electrolyte interface (SEI) of the anode, cathode, and electrolyte, which can result in fires or explosions [6–9].

Lithium-ion battery modeling has evolved significantly, beginning with the foundational work by Doyle and Newman [10,11]. Their “pseudo-2D” (P2D) model incorporates one-dimensional cell layers and solid lithium diffusion in electrode particles, which require about 40 parameters for accurate representation. While highly detailed, this complexity limits its practicality in engineering. For low to moderate currents, the model is often simplified using a single-particle (SP) approach, which assumes uniform conditions across porous electrodes and uses lumped resistance terms to enhance computational efficiency [12]. Different studies have utilized the single-particle (SP) model and the more comprehensive pseudo-2D (P2D) model as foundational frameworks to investigate the thermal behavior of lithium-ion batteries. These models serve as critical tools in analyzing heat generation mechanisms, temperature distribution, and their effects on battery performance and safety [13–17].

Thermal runaway in Li-ion cells involves a chain reaction mechanism triggered by abnormal temperature increases under abusive conditions. This process is fueled by the Heat–Temperature–Reaction (HTR) loop. Initially, abnormal heat generation raises the cell’s temperature, initiating side reactions like the decomposition of the solid electrolyte interface (SEI). These reactions release additional heat, perpetuating the HTR loop until the cell undergoes thermal runaway [4]. There are three types of abuse that trigger thermal runaway: mechanical, electrical, and thermal abuse. Mechanical abuse refers to physical damage to the battery, such as crushing and penetration, which can compromise the battery’s structural integrity and lead to ignition. Examples of electrical abuse are high currents, overcharging, over-discharging, or short-circuiting. Thermal abuse occurs when a Li-ion battery is exposed to external temperatures outside its safe operating range, which can happen due to environmental conditions, poor thermal management, or external heat sources.

Modeling thermal runaways in lithium-ion batteries is a critical area of research aimed at understanding and mitigating safety risks associated with battery operation. One common strategy involves the development of electrochemical–thermal models, such as those based on the Newman framework [10,11], which integrate electrochemical reactions with heat generation and transport mechanisms within the battery cell. These models typically consider factors like heat generation from electrochemical reactions, ohmic heating due to internal resistance, and heat dissipation through conduction, convection, and radiation. Thermal runaway modeling has also advanced, with Hatchard et al. [14] developing a model focusing on side reactions during runaway events, which are validated through oven tests. Kim et al. [9] expanded this to a 3D framework, incorporating additional reactions, thus inspiring further research into the thermal behavior and safety of Li-ion batteries. Another significant aspect is the incorporation of thermal abuse models, which simulate extreme conditions such as overcharging or external heating to predict how these conditions can trigger thermal runaway [15–17]. Talele et al. [15] used a thermal runaway numerical model to study the trigger point evolution in prismatic cells with different cathode chemistries (NMC, LFP, and LCO) under varying ambient temperatures. They employed nail penetration-assisted thermal abuse testing and empirical correlations to simulate the source term. By ANOVA-based statistical evaluation, they found ambient temperature to be the most influential factor on trigger time for both natural and forced convection conditions. Jelly roll thickness and heat transfer coefficient (HTC) were identified as additional critical parameters. Azuaje–Berbecí et al. [16] proposed a multilayered electrochemical–thermal model designed to predict heat generation, battery temperature, voltage, and the potential

for thermal runaway during lithium-ion battery charge/discharge cycles under various operating conditions. Their findings revealed that cyclic charging and discharging can elevate the battery temperature to levels capable of triggering thermal runaway. Özdemir et al. [17] investigated the thermal behavior of lithium-ion cells under both normal and abusive operating conditions through experimental and numerical approaches. They developed an electrochemical–thermal model to simulate temperature and voltage variations during discharge processes. The model was enhanced to incorporate the effects of temperature-dependent heat generation by utilizing Arrhenius equations.

Most battery modeling for thermal runaway focuses on a fresh battery and does not contain any aging-related mechanism, which is an important contributing factor that may heighten the risk [18,19]. Aging refers to the degradation of the cell over time, which is evidenced by battery performance. To understand the aging of a Li-ion battery, three main questions need to be answered: What factors cause battery aging? What happens to a battery during aging? And what are the consequences of the aging process?

There are two main categories of aging: cycling aging and calendar aging. During the operation of a battery in an electrical application such as in an electric vehicle, aging occurs primarily due to the repeated charging and discharging phases called “cycling aging”. This type of lithium-ion battery aging is significantly affected by key operating conditions such as temperature, charge/discharge current rates (C-rate), depth of discharge (DOD), and mechanical stress [20]. Battery aging can also occur while the battery is at rest in a process known as calendar aging. During this period, the battery is exposed to ambient temperatures without active thermal management, potentially leading to more aggressive aging due to exposure to higher or lower ambient temperatures than those reached during cycling when the thermal management system can better control the temperature. This rate of degradation is influenced by factors such as the battery’s state of charge (SOC) and the duration of storage [21]. Lithium-ion battery degradation typically follows four key modes: loss of Lithium inventory, loss of active material in the negative and positive electrodes [22], and conductivity loss [20]. Lithium ions can be consumed inside reactions such as solid electrolyte interface (SEI) layer growth, electrolyte decomposition, or lithium plating, causing lithium shortage for cycling. The active material in the anode and cathode becomes unavailable for lithium insertion due to mechanisms such as particle cracking, loss of electrical contact, or blockage by resistive surface layers. It is worth mentioning that these mechanisms have different paths and effects depending on battery chemistry, and they can affect the performance of the cell through three main factors—capacity, power, and internal resistance—which have been the preferred aging indicators of lithium-ion batteries. Structural disorder, loss of active material, crystal distortion, and mechanical stress contribute to capacity and power fading, while surface layer formation, such as in lithium plating and SEI layer growth, increases impedance and resistance [21]. These aging effects alter the physical and chemical properties of cell components, significantly influencing the thermal behavior of lithium-ion batteries. However, there are fewer studies on the thermal safety of aged lithium-ion cells, especially those using numerical methods, compared to fresh cells.

In the study by Fleischhammer et al. [23], the impact of cyclic aging on the thermal behavior of Li-ion cells was investigated, and the results revealed that cells subjected to high-rate cycling exhibited the same thermal behavior as fresh cells. In contrast, Wu et al. [18] conducted an experimental study using ARC tests to investigate how low-temperature aging affects the thermal behavior of Li-ion batteries. The results showed that low-temperature cycling significantly influences TR performance, leading to a faster onset of thermal runaway and increased self-heating rates at the same temperature. Another study [24], conducted to investigate the influence of calendar aging on the thermal stability

of a commercial Li-ion cell, revealed that the self-heating onset temperature of aged cells was much lower than that of fresh cells. Garcia et al. [19] examined the thermal runaway (TR) behavior of fresh and aged NMC 811 batteries using ARC testing at different SOCs. Their findings showed that higher SOC led to earlier exothermic reaction detection, highlighting the rapid escalation risk at high SOC conditions. Guo et al. [25] investigated the effects of aging on the safety performance of commercial 18650 lithium-ion batteries by subjecting them to fast charge/discharge cycles and conducting thermal abuse tests. The results revealed that aged cells exhibited improved thermal stability compared to fresh cells and had significantly higher thermal runaway temperatures. This study suggests a greater likelihood of thermal runaway propagation in the module of aged cells used in applications such as electric vehicles due to the higher temperature of the thermal runaway. Zhang et al. [26,27] conducted a comprehensive investigation into the thermal safety evolution of lithium-ion batteries during high-temperature aging. Their study revealed that both high-temperature cyclic aging and calendar aging result in similar thermal hazard and degradation mechanisms. The findings showed that high-temperature aging significantly reduces the thermal stability of the cells. The study observed that the gas released during the aging process reduces the amount of gas available for release during a potential thermal runaway event. Although aging decreases the cells' thermal stability, it also mitigates the overall thermal hazards posed by the batteries through this gas release.

Abada et al. [28] developed a 3D model for an aged battery. They considered the SEI growth as the main cause of calendar aging in Li-ion cells and incorporated this concept into the 3D thermal model to investigate the thermal behavior of a cell subjected to external heating. The results showed that SEI growth hinders the anode decomposition and consequently increases the onset temperature of thermal runaway. However, their model did not consider the effects of SEI growth on the increase in the internal resistance of the cell. Grandjacques et al. [29] developed a semi-empirical model for predicting the thermal behavior of an aged lithium-ion cell based on an Arrhenius kinetic equation. Zhao et al. [30] developed a thermal runaway model for lithium-ion batteries subjected to low-temperature cycling. Their model incorporates an exothermic reaction between metallic lithium and the electrolyte to account for aging effects. The results indicated that aging slightly increases the total heat generated during thermal runaway, but the impact remains relatively small. In the study by Pastor et al. [31], the impact of aging on thermal runaway behavior was experimentally investigated for lithium-ion batteries with NMC and LFP cathode chemistries using Accelerating Rate Calorimetry (ARC) tests. Aged batteries were subjected to external heating abuse to evaluate thermodynamic parameters related to thermal runaway. A computational model was also developed using GT-Autolion software for further analysis. Results indicated that aged batteries released less heat during thermal runaway when triggered by external heating. This reduced heat generation was attributed to SEI growth, a key aging mechanism causing capacity to fade, which decreases the availability of lithium and electrolyte in the anode, thus diminishing the exothermic reactions during thermal runaway. Kabra et al. [32] utilized a combination of experimental and modeling approaches to explore the impact of aging mechanisms on the thermal stability of Li-ion cells. They developed a physics-based aging model to study degradation processes such as lithium plating, SEI layer growth, and active material loss during cycling. By integrating insights from this aging model with Accelerating Rate Calorimetry (ARC) experiments, they created a degradation-aware thermal stability model capable of predicting the onset and intensity of thermal runaway (TR) in Li-ion cells. The findings revealed that while SEI decomposition contributes to earlier TR onset, additional SEI growth can mitigate anode–electrolyte reactions, delaying TR. In contrast, for cells cycled at low temperatures, TR was predominantly driven by lithium plating

and the subsequent reaction between plated lithium and the electrolyte. These studies mainly consider the external heat as a trigger for thermal runaway, but they did not consider the effect of high current or other electrical abuse conditions, possibly resulting in a thermal runaway.

This study focuses on developing an electrochemical–thermal coupled model that accounts for side reactions, which lead to thermal runaway, while also trying to include aging effects. The model is validated using experimental data for fresh NMC Li-ion batteries and for aged NCA Li-ion batteries [33]. It aims to simulate the thermal behavior of aged cells and to explore the impact of external factors, such as high current rates, and internal factors, including impedance and capacity variations involved in aging effects, on thermal runaway initiation. Statistical analysis is used to evaluate the influence of these conditions on the thermal behavior of an NMC cell. The study focuses on cylindrical NMC and NCA Li-ion batteries due to their widespread applications, and it consists of three parts:

- Development of the electrochemical–thermal coupled model;
- Validation of the model;
- Statistical analysis for finding the most influential factors on an aged cell’s thermal behavior.

2. Methods

2.1. Geometry

The battery under study is a cylindrical lithium-ion battery with a length of 65 mm, a radius of 9 mm, a container thickness of 0.25 mm, and a mandrel thickness of 2 mm and it has been represented by using a 2D geometry with axial symmetry feature. Figure 1 represents the schematic of the geometry. The three main parts of the cell, represented by the adopted geometry, are as follows:

- The container: it is wrapped around the active volume of the cell; the heat-transfer between the battery and the external ambient happens through this part, made of steel.
- The battery’s active material: the different parts where the electrochemical reactions occur are assumed to be lumped in this part.
- Mandrel: it is the isolator around which the battery cell sheets are wound.

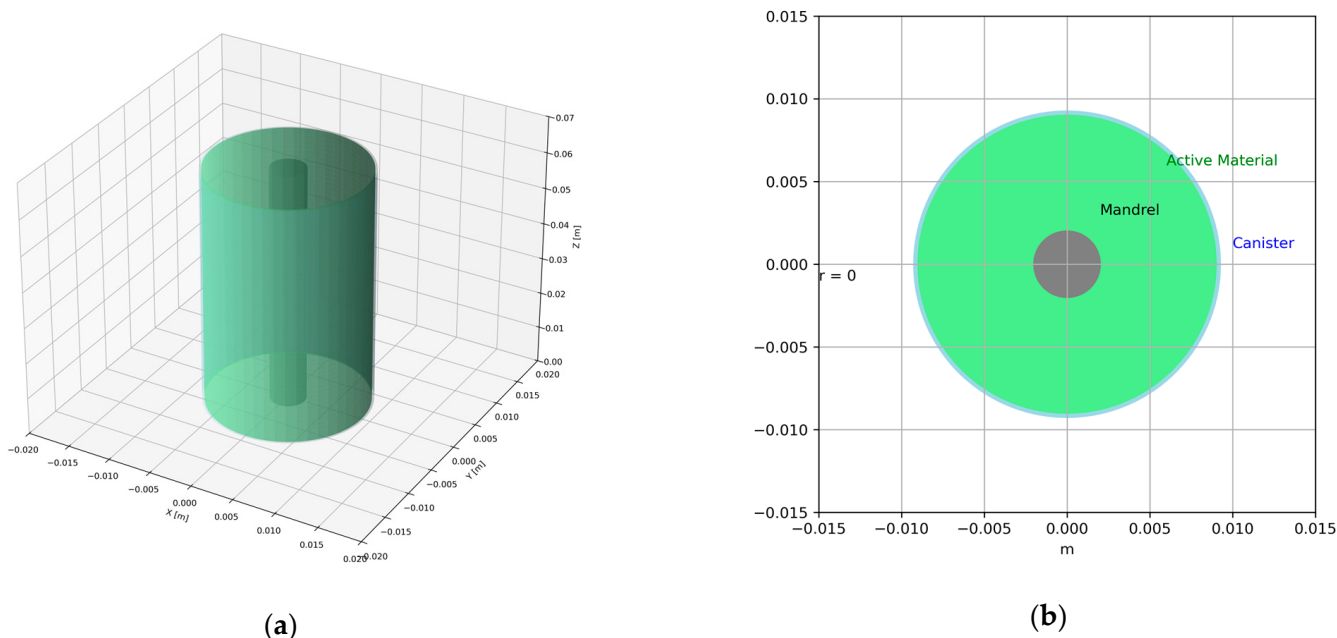


Figure 1. Schematic of Li-ion Battery: (a) 3D view; (b) Top cross section radial view.

2.2. Mass Balance and Electrochemical Reactions

In this work, the electrochemical behavior of the Li-ion battery is modeled using the single-particle (SP) approach, a simplified lumped model derived from the more detailed pseudo-2D (P2D) model. In the selected model, each electrode is represented by spherical intercalation particles of uniform size, and the current distribution is assumed to be uniform across the electrode thickness. This simplification captures the essential physics of lithium intercalation while significantly reducing computational complexity, making it well-suited for coupled thermal simulations. The mass balance is represented in Equations (1) and (2).

$$\frac{\partial c_{s,j}}{\partial t} + \frac{15D_{1,j}}{R_j^2} (c_{s,j} - \bar{c}_{1,j}) = 0 \quad (1)$$

$$\frac{15D_{1,j}}{R_j} (\bar{c}_{1,j} - c_{s,j}) + \frac{J_j}{A_j F} = 0 \quad (2)$$

where $c_{s,j}$ is average concentration and $\bar{c}_{1,j}$ is the concentration at the surface of the sphere; the initial condition is given by Equation (3):

$$c_{s,j}|_{t=0} = c_{1,j,0} \quad (3)$$

where $c_{1,j,0}$ denotes the concentration of lithium inside electrode 'j' at the beginning of charge or discharge. The surface concentration is then used in place of $c_{1,j}|_{r=R_j}$ in the flux expressions. The battery cell voltage E_{cell} is defined as in Equation (4) [34]

$$E_{cell} = E_{OCV}(SOC_{average}) + \eta_{IR} + \eta_{act} + \eta_{conc} \quad (4)$$

Using spherical symmetry for spherical particles, the diffusion process is defined by Equation (5)

$$\tau \frac{\partial SOC}{\partial t} = -\nabla \cdot (-\nabla SOC) \quad (5)$$

The diffusion time constant, τ (in seconds), characterizes the timescale for diffusion within the particle. The spatial domain represents an average particle in the electrode, with $X = 0$, $X = 1$ corresponding to the particle center and surface, respectively. The boundary conditions at these locations are specified as follows:

$$\nabla SOC = 0|_{X=0} \quad (6)$$

$$\nabla SOC = \left. \frac{\tau I_{cell}}{N_{shape} Q_{cell,0}} \right|_{X=1} \quad (7)$$

For spherical particles, the parameter N_{shape} is set to 3. The initial state of charge (SOC) of the cell is defined by SOC_0 . The surface SOC ($SOC_{surface}$) is determined at the particle surface ($X = 1$), while the average SOC ($SOC_{average}$) is obtained by integrating over the particle volume, with appropriate consideration for spherical coordinates, as described in Equation (8).

$$SOC_{average} = \frac{\int_0^1 SOC 4\pi X^2 dX}{\int_0^1 4\pi X^2 dX} = 3 \int_0^1 SOC \cdot X^2 dX \quad (8)$$

The lumped voltage loss due to ohmic processes within the electrolyte and electrodes used in Equation (4) is expressed by Equation (9)

$$\eta_{IR} = \eta_{IR,1c} \frac{I_{cell}}{I_{1C}} = R_{ohm} I_{cell} \quad (9)$$

where $\eta_{IR,1C}$ (V) is the ohmic overpotential at 1C, I_{cell} is the applied current, and the 1C current, I_{1C} (A), is defined as Equation (10) where $Q_{cell,0}$ (C) is the battery cell capacity. This equation highlights the role of ohmic resistance Rohm in determining the internal resistance voltage drop η_{IR} . Rohm (ohmic resistance) is a specific type of resistance that obeys Ohm's Law and excludes any reactive components. It is generally constant across frequencies and provides a purely resistive behavior. This factor, the internal resistance, and capacity are the main indicators of the aged cell.

$$I_{1C} = \frac{Q_{cell,0}}{3600} \quad (10)$$

The dimensionless charge exchange current, J_0 , is utilized to characterize the lumped voltage loss linked to charge transfer reactions occurring on the surfaces of both the positive and negative electrodes. This relationship is expressed in Equation (11), where R represents the molar gas constant, T is the temperature, and F is Faraday's constant.

$$\eta_{act} = \frac{2RT}{F} \sinh^{-1} \left(\frac{I_{cell}}{2J_0 I_{1c}} \right) \quad (11)$$

Finally, the lumped voltage loss associated with concentration overpotential is defined as in Equation (12)

$$\eta_{conc} = E_{OCV}(SOC_{surface}) - E_{OCV}(SOC_{average}) \quad (12)$$

2.3. Energy Balance

The energy balance governing the thermal behavior of the single cell is represented in Equation (13), where ρ is the density of the system, c_p is the specific heat capacity, k is the thermal conductivity

$$\frac{\partial(\rho c_p T)}{\partial t} = -\nabla(k\nabla T) + Q_{TR} + I(\eta_{IR} + \eta_{act} + \eta_{conc}) \quad (13)$$

The term $I(\eta_{IR} + \eta_{act} + \eta_{conc})$ in Equation (13) refers to activation, ohmic, and concentration (entropic) heat generation rate in batteries, which also can be calculated as defined by the literature [35,36]; the latter one is neglected by the uniform concentration of electrolyte in the lumped assumption. At an elevated temperature, side reactions will happen, so that Q_{TR} represents the overall heat generated by these side reactions which can be calculated by Equation (14), where S_{SEI} , S_{ne} , S_{pe} , S_{ed} and S_{bd} are the heat sources for SEI decomposition, the negative electrode-electrolyte reaction (NE), the positive electrode-electrolyte reaction (PE), the electrolyte decomposition reaction (ED), and binder reaction (BD), respectively [9]:

$$Q_{TR} = S_{SEI} + S_{ne} + S_{pe} + S_{ed} + S_{bd} \quad (14)$$

At high current densities, concentration gradients in the electrolyte become significant. To reduce the calculations, the real sandwich-type structure of the cell has been replaced, assuming a pseudo-homogeneous active material; because of this assumption, the thermal properties of the model have to be calculated based on their specific values, according to the following equations [37]:

$$k_{T,ang} = \frac{\sum L_i k_{T,i}}{\sum L_i} \quad (15)$$

$$k_{T,r} = \frac{\sum L_i}{\sum L_i / k_{T,i}} \quad (16)$$

where L_i is the thickness of each layer of the cell, and $k_{T,i}$ the thermal conductivity of the materials constituting these layers. In particular, $k_{T,ang}$ and $k_{T,r}$ are the thermal conductivities in the cylinder length direction and radial direction, respectively. For the other physical properties, similar equations can be used.

As mentioned before, at increasing temperatures, exothermic side reactions will happen (SEI decomposition, anode–electrolyte reaction, and cathode conversion) so that additional heat will be released. The kinetics of these reactions will be represented by the following Arrhenius-type equation [38]:

$$R_i = A_i \exp\left(-\frac{E_{a,i}}{RT}\right) c_i^{ni,1} (1 - c_i)^{ni,2} \quad (17)$$

where c_i is the dimensionless concentration calculated as

$$\frac{dc_i}{dt} = \begin{cases} R_i & \text{for PE} \\ -R_i & \text{for others} \end{cases} \quad (18)$$

The heat generated by each reaction will be subsequently calculated as follows:

$$S_i = H_i W_i R_i \quad (19)$$

where S_i is the heat release rate for the i th side reaction (W/m^3), H_i is the reaction heat for the i th side reaction (J/kg), W_i is the specific active substance content of the i th side reaction (kg/m^3).

For solving the energy balance, the following boundary conditions are needed:

- At $t = 0$ (beginning of the simulation), the battery (all parts) and the surrounding area are at a steady state at the same constant ambient temperature (298.15 K).
- At $r = 0$, a symmetrical boundary condition is used, i.e., the derivation of the temperature with respect to the radius equals zero.
- On the external surface, i.e., at $r = R$, at $z = 0$, and $z = L$, the heat conducted through the inner volumes of the cell is transferred to the external ambient air by natural convection, and the corresponding heat transfer coefficient has been assumed equal to 10 $\text{W}/\text{m}^2\text{K}$ (this factor is mainly used for fitting purposes).

The simulations will be carried out in Comsol Multiphysics 6.3 and conducted in two modes: charging and charge/discharge cycle. The charging and cycling will be performed using a constant current. As mentioned, two battery chemistries have been used for this study, and the related model parameters are extracted from the literature [22,39,40] and shown in Tables 1 and 2.

Table 1. Physical properties of different components of a Li-ion cell [39] used in Energy balance.

Component	Thermal Conductivity ($\text{W}/\text{m K}$)	Heat Capacity (J/kg K)	Density (kg/m^3)	Thickness of Component Layer (m)
Negative Current Collector	398	385	8933	7×10^{-6}
Anode	1.04	1437	2660	5.5×10^{-5}
Separator	0.33	1978	492	3×10^{-5}
Cathode (NMC)	1.5	710	2380	5.5×10^{-5}
Cathode (NCA)	6.10	651	4581	5.5×10^{-5}
Positive Current Collector	238	903	1500	1×10^{-5}

Table 2. Physical and kinetic parameters adopted in the side reactions [22].

<i>i</i> th Reaction	A_i (s^{-1})	$E_{a,i}$ (J/mol)	H_i (J/kg)	$c_{i,0}$	$n_{i,1}$	$n_{i,2}$	W_i (kg/m^3)
SEI	1.667×10^{15}	1.35×10^5	2.57×10^5	0.15	1	0	875
NE	2.5×10^{13}	1.35×10^5	1.714×10^6	0.75	1	0	875
PE (NMC)	2.25×10^{14}	1.54×10^5	7.9×10^5	0.04	1	1	1293
PE (NCA)	7.25×10^{16}	1.3×10^5	2.18×10^5	0.04	1	1	1274

2.4. Aging

Internal resistance is a well-established and effective indicator for battery aging because it encapsulates the cumulative impact of various degradation mechanisms. As a battery ages, processes such as SEI layer growth, active material loss, electrolyte decomposition, and structural changes within the electrodes contribute to an increase in internal resistance. This rise in resistance not only reflects these individual degradation phenomena but also directly affects battery performance by reducing power output and increasing voltage drops. Therefore, by monitoring changes in internal resistance, one can obtain an integrated measure of battery health that is sensitive to a range of aging mechanisms. This makes internal resistance a practical and reliable parameter for assessing battery aging and predicting the remaining useful life of the cell.

2.5. Statistical Analysis

To identify the most influential factors affecting the thermal behavior of the cell, the *p*-value will be analyzed using an analysis of variance (ANOVA). The *p*-value is commonly used to test the null hypothesis (H_0), which assumes no effect or no difference. It is determined based on the F- or t-score and is compared against a known probability distribution to assess the likelihood of obtaining the observed results if H_0 were true. It is important to note that the *p*-value does not represent the probability of a specific factor but rather the likelihood of rejecting or failing to reject a hypothesis. In this study, a low *p*-value (≤ 0.05) indicates a statistically significant result, leading to the rejection of H_0 , suggesting that the factor has a meaningful impact on thermal behavior.

The ANOVA in this study is performed using a design of experiments (DOE). A full factorial design is used with three four-level factors to investigate the effects of capacity, ohmic resistance, and charging rate on thermal behavior, which consist of 64 simulations reported in Table 3. To analyze thermal behaviour, two key outputs have been chosen: the average cell temperature and the temperature derivative over time, both in a battery charged at 10, 50, and 100% state of charge (SOC). The cell's initial SOC is set near zero (0.05), and the initial (ambient) temperature is considered 298.15 K. The ANOVA will be carried out in Python v3.9 and the open library pyDOE2 v1.3.0, and *p*-values with confidence levels of 95% will be used to find the best features presenting the related results.

Table 3. Selected parameters used in the simulations of the Full Factorial design.

Run Order	Internal Resistance (mOhm)	Capacity (Ah)	Current C-Rate (A)	Run Order	Internal Resistance (mOhm)	Capacity (Ah)	Current C-Rate (A)	Run Order	Internal Resistance (mOhm)	Capacity (Ah)	Current C-Rate (A)
1	10	1	1	26	20	3	3	51	30	1	8
2	20	1	1	27	30	3	3	52	40	1	8
3	30	1	1	28	40	3	3	53	10	2	8
4	40	1	1	29	10	5	3	54	20	2	8
5	10	2	1	30	20	5	3	55	30	2	8
6	20	2	1	31	30	5	3	56	40	2	8
7	30	2	1	32	40	5	3	57	10	3	8
8	40	2	1	33	10	1	6	58	20	3	8
9	10	3	1	34	20	1	6	59	30	3	8
10	20	3	1	35	30	1	6	60	40	3	8

Table 3. Cont.

Run Order	Internal Resistance (mOhm)	Capacity (Ah)	Current C-Rate (A)	Run Order	Internal Resistance (mOhm)	Capacity (Ah)	Current C-Rate (A)	Run Order	Internal Resistance (mOhm)	Capacity (Ah)	Current C-Rate (A)
11	30	3	1	36	40	1	6	61	10	5	8
12	40	3	1	37	10	2	6	62	20	5	8
13	10	5	1	38	20	2	6	63	30	5	8
14	20	5	1	39	30	2	6	64	40	5	8
15	30	5	1	40	40	2	6				
16	40	5	1	41	10	3	6				
17	10	1	3	42	20	3	6				
18	20	1	3	43	30	3	6				
19	30	1	3	44	40	3	6				
20	40	1	3	45	10	5	6				
21	10	2	3	46	20	5	6				
22	20	2	3	47	30	5	6				
23	30	2	3	48	40	5	6				
24	40	2	3	49	10	1	8				
25	10	3	3	50	20	1	8				

2.6. Machine Learning Analysis

To find a correlation between exercised features in analytical analysis, a linear regression model will be fitted for different sets of results. The basic model is presented in Equation (20).

$$a_0 + a_1x_1 + a_2x_2 + \dots + a_nx_n = \hat{y} \quad (20)$$

where the a_0, a_1 to a_n are coefficients for x_1 to x_n features and \hat{y} is the predicted output. If the relationship between features and output is not linear, y_{actual} and \hat{y} have different values, so the difference between these two values needs to be minimized. The objective function is presented in Equation (21). To find the best fit, the coefficients are updated in an iterative approach to satisfy the objective function.

$$\text{minimize} \sum_{i=1}^n (\hat{y} - y_{actual})^2 \quad (21)$$

As a battery ages, its internal resistance increases, and if it exceeds a critical threshold, it can trigger rapid temperature escalation and increase the risk of thermal runaway. Identifying this threshold is crucial for ensuring battery safety. By defining this limit, proactive measures such as thermal management and early fault detection can be implemented to prevent hazardous conditions, extend battery lifespan, and maintain safe operation in applications like electric vehicles and energy storage systems. To determine this threshold, a classification task will be performed using internal resistance, current, and capacity as input features, with thermal runaway occurrence as the target variable. A logistic regression model is selected for its versatility and strong predictive capabilities. The logistic regression function is presented in Equation (21), requiring an iterative process to satisfy Equation (20) for the predicted \hat{y} in Equation (21), which is the probability. The dataset will be divided into training and testing sets to ensure proper model evaluation and prevent overfitting. Once trained, the model can be used to determine the internal resistance threshold by fixing the output and other feature values, leading to the derivation of Equation (23) from Equation (22) for this specific task.

$$\hat{y} = \frac{e^{b_0 + b_1x_1 + \dots + b_nx_n}}{1 + e^{b_0 + b_1x_1 + \dots + b_nx_n}} \quad (22)$$

$$x_1 = -\frac{1}{b_1} \left(\ln \left(\frac{1}{\hat{y}} - 1 \right) + (b_0 + b_2x_2 + b_3x_3) \right) \quad (23)$$

These tasks will be carried out in Python with the open library scikit-learn. To check the performance of the fitted values, R-squared for linear regression and confusion matrix for logistic regression will be used.

2.7. Validation

2.7.1. Charge Testing: Voltage Comparison

The proposed model has been validated using experimental data from the literature [41], referred to as a commercial 26,650 NCM/graphite cell with a capacity of 5 Ah, with cell dimensions of 26 mm in diameter and 65 mm in height. The study evaluated the cell's performance at charge rates of 0.2C, 0.5C, and 1C, with a cut-off voltage set at 4.2 V. Figure 2 illustrates the validation of the electrochemical model, confirming the cell's performance during the charging process without triggering side reactions. The results demonstrate that the simulated cell voltage closely aligns with the experimental data throughout the charging period, highlighting the model's accuracy. Additionally, as shown in Figure 2, the voltage derivation increases over time with higher charging currents. This trend is accurately captured by the model. The small discrepancies between the experimental and simulated results are attributed to the simplifying assumptions of a single-particle model, which does not fully account for the complexities of a real cell.

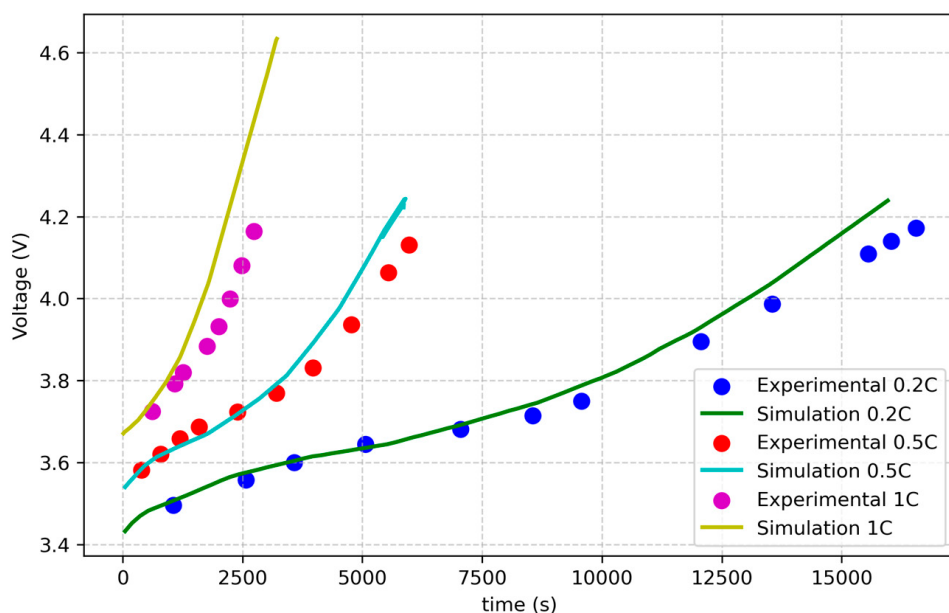


Figure 2. Charging test for 0.2C, 0.5C, and 1C simulation vs. experiment [41].

2.7.2. Charge Testing: Temperature Comparison

The proposed model was then validated using experimental data to check the temperature behavior at constant current charging rates of 1C and 8C. For this purpose, the study by Dong et al. [42] was chosen, as it provided temperature data at various charging and discharging rates. In the experiments, the temperature monitoring point was positioned at the center of the outer surface, and in the simulation, the same point on the surface was adopted. The cell under investigation is a cylindrical spiral 18650 battery with an NCM cathode, a radius of 9 mm, a height of 65 mm, and a nominal capacity of 1.5 Ah. Figure 3 compares the simulated and experimental cell temperatures during the 1C and 8C charging processes, starting with an initial SOC of approximately 0.05. The results demonstrate that at a constant SOC, the cell's temperature increases more significantly at higher charging rates: as expected, the 8C charge rate leads to a greater temperature rise and higher temperature derivation over time compared to the 1C charge rate. The

data show a strong correlation between the simulation and experimental results, indicating good agreement. By comparing the proposed numerical model with experimental results from the literature, it can be concluded that a single-particle electrochemical model coupled with a heat balance is an effective approach to understanding the thermal behavior of lithium-ion batteries.

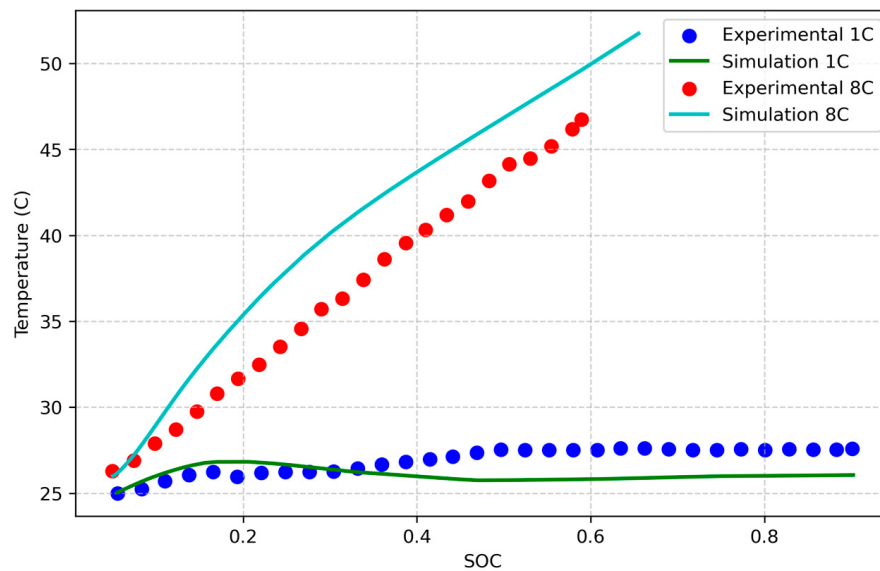


Figure 3. Temperature vs. SOC in Charging test for 1C and 8C simulation vs. experiment [42].

2.7.3. Overcharging and Thermal Runaway

The third validation test for the proposed model focused on the thermal behavior of a cell during overcharging. The model has been validated against experimental data to analyze the temperature behavior during constant current charging at rates of 1C, 2C, and 3C, as well as under overcharging conditions beyond full cell capacity. The study by Liu et al. [43] was selected due to its comprehensive temperature data for different overcharging rates. Their experiments utilized 18650 NCM523 lithium-ion batteries with a capacity of 2.6 Ah, a radius of 9 mm, and a height of 65 mm. Testing was conducted at an ambient temperature of about 298.15 K under natural ventilation. Throughout the experiments, and as reported in the literature, the surface temperature of the battery was monitored, and the simulation recorded temperatures at the center of the outer surface of the cell. Figure 4 shows that overcharging beyond a certain point can lead to thermal runaway. This phenomenon is attributed to electrochemical and side reactions, as discussed previously, causing a catastrophic increase in the heat released by the cell. The figure clearly illustrates that higher charging rates significantly reduce the time to thermal runaway. One limitation of the model is its omission of gas release and ignition processes, which contributes to discrepancies between the simulated and experimental results. These mechanisms are more prominent at lower C-rates, where the system has more time to dissipate heat, resulting in less severe temperature buildup, particularly evident under 1C overcharge conditions. Interestingly, the model demonstrates better agreement with experimental data at higher current rates. Given this observation and the relatively lower error margins at moderate currents, the study places greater emphasis on moderate C-rate scenarios, which will be further discussed in the following sections. Overall, Figure 4 supports the model's effectiveness in analyzing thermal runaway behavior in lithium-ion batteries, showing good alignment with the experimental trends.

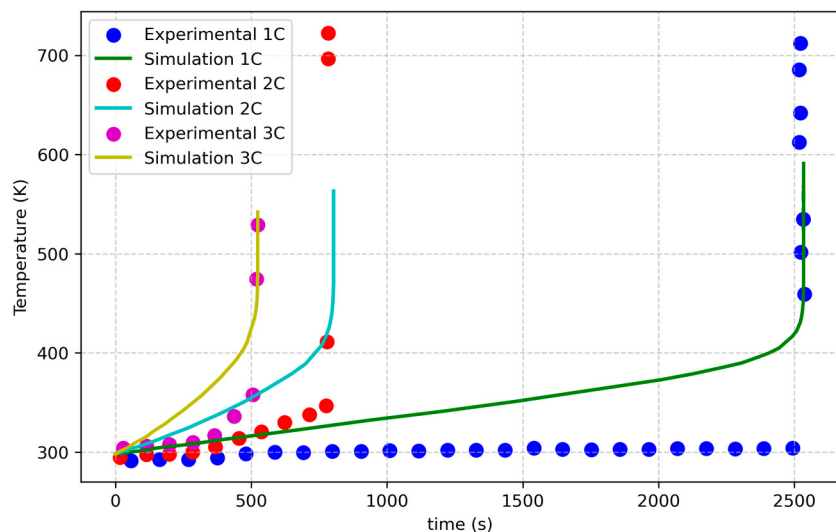


Figure 4. Overcharging test for 1C, 2C, and 3C simulation vs. experiment [43].

2.7.4. Aged Cell

The fourth set of validation runs was performed to assess the voltage and temperature trend predictions for aged cells. The dataset [33] was collected from a custom-built battery prognostics testbed at the NASA Ames Prognostics Center of Excellence (PCoE), and the study involved testing Li-ion batteries under three different operational profiles: charge, discharge, and Electrochemical Impedance Spectroscopy (EIS). The data used for the validation refer to cell No. 7 in the NASA dataset, which is an NCA 18650-sized rechargeable battery with 2 Ah nominal capacity, discharged with -1.98 A from a fully charged state. The ambient temperature was set at 297.5 K, and the battery cycled 168 times. Figure 5 represents the cell's thermal behavior during discharge at the 19th cycle and 168th cycle; both the experimental data and the simulations use the fitted internal resistance value, which shows a relation to the aged battery trend. Simulations with fitted internal resistance resulted in 0.4257689 and 0.4653298 RMSE for the 19th and 168th cycles, respectively. The figure shows a very good agreement between simulations and experimental data, so it can be concluded that the developed model is capable of properly predicting the thermal behavior of an aged cell.

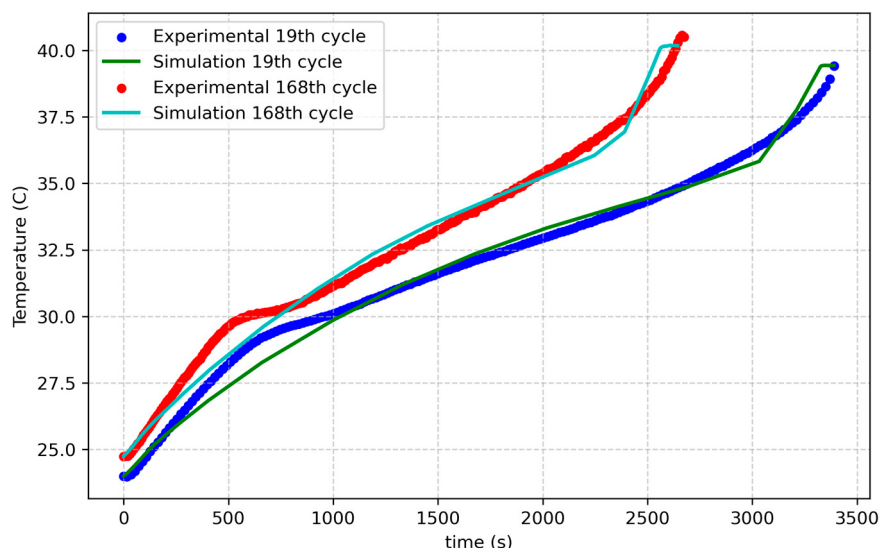


Figure 5. Fresh and aged cell temperature profile [33].

3. Results and Discussion

Figure 6 illustrates the results of the first simulation during charging. Initially, the cell's state of charge (SOC) was near zero, and the cell was charged using a 1C current to reach a fully charged state (Figure 6a). As shown in Figure 6b, the cell temperature increases steadily due to the heat generated by electrochemical reactions. In Figure 6b, at the start of the charging, heat dissipation to ambient is poor due to the fact that surface temperature is close to ambient temperature. After a while, the temperature increment reaches the surface of the cell, heat dissipation becomes larger, and the temperature almost reaches a steady state. Figure 6c shows that the temperature in the middle of the cell is higher compared to other regions. This phenomenon is related to the geometry of the cell, as heat accumulates more at the core due to limited pathways for thermal dissipation in cylindrical battery designs.

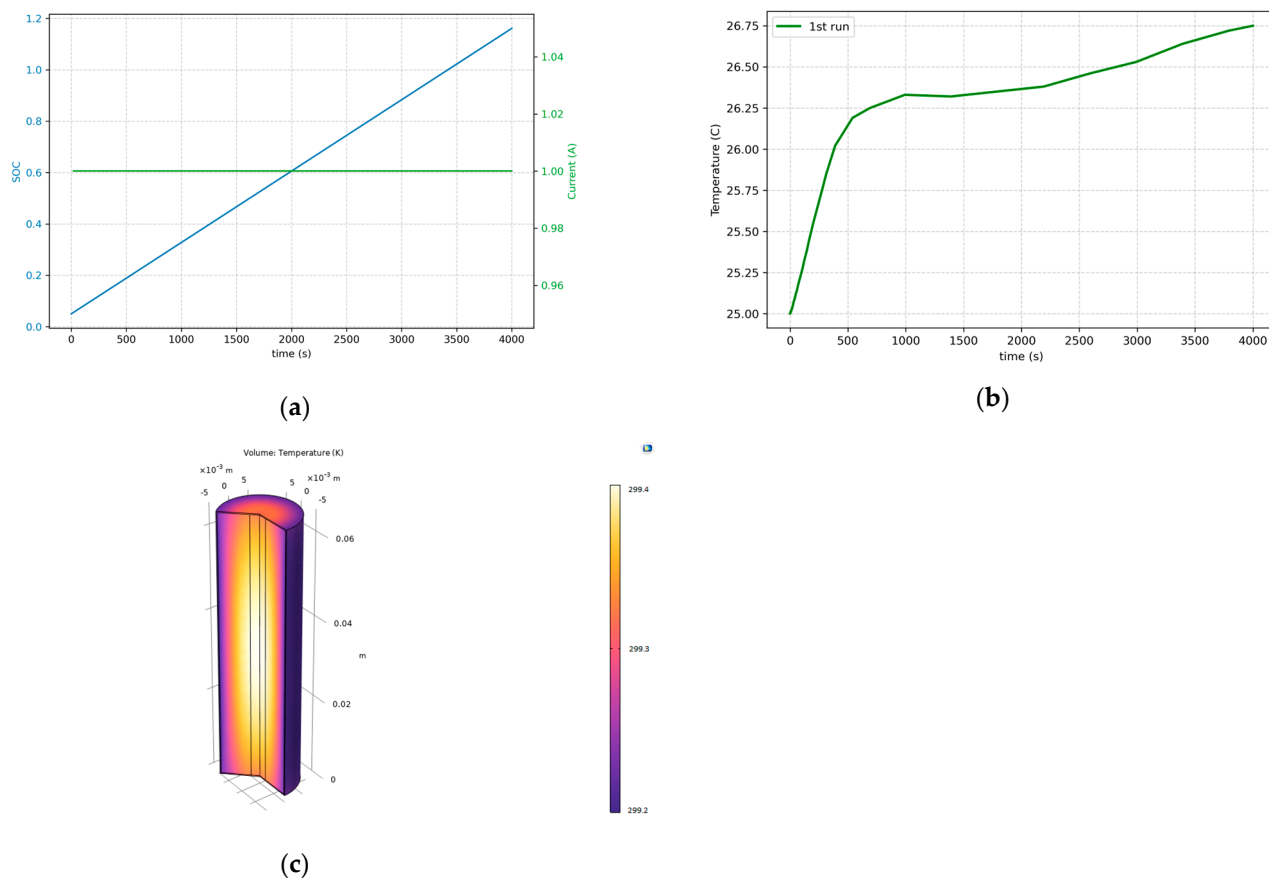


Figure 6. Simulation of the cell number 1 (1 Ah, 1C and 10 mOhm): (a) state of charge and current vs. time; (b) mean temperature derivation of cell vs. time; (c) temperature distribution in the cell at $t = 1500$ s.

Figure 7 shows the results of the charging/discharging cycles of simulation no. 33 in which a cell with 1 Ah capacity and 10 mOhm internal resistance was charged/discharged using a constant current of 6C. Figure 7a illustrates the voltage and current of the cell. In the charging and discharging phases, the current is positive and negative, respectively, and voltage increases from around 2.7 V to 4.2 V in charging and vice versa in discharging. Figure 7b presents the thermal behavior of the cell during this process: at the beginning and after a few cycles, temperature increases due to heat generation by reversible entropy losses [44]; after the temperature has reached a certain point, heat dissipation to the

environment and heat generation within the cell due to charging/discharging almost balance each other and the temperature trend becomes nearly constant.

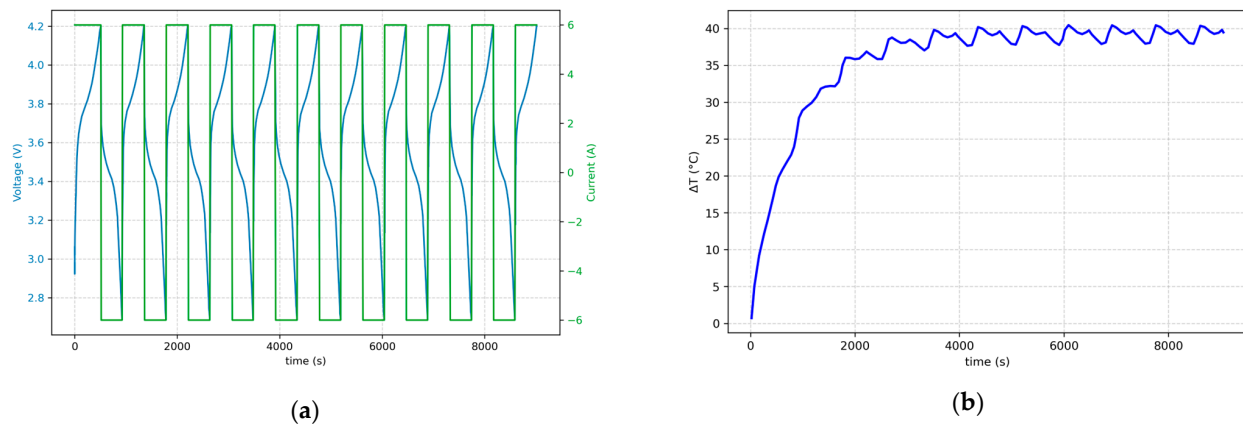


Figure 7. Simulation n. 33 during cycling (1 Ah, 6C, and 10 mOhm): (a) voltage and current vs. time; (b) mean temperature increase vs. time.

3.1. Influence of Charging Rate on Thermal Behavior

Figure 8 illustrates the temperature trends for four simulations with 1C, 3C, 6C, and 8C charging rates and fixed resistance and cell capacity. As shown, the charging rate has a significant impact on the temperature behavior of lithium-ion cells, with higher charging rates resulting in increased thermal effects. This trend is expected and aligns with the theoretical understanding of heat generation in electrochemical systems. As illustrated by Equation (13), the rate of heat generation is directly influenced by the charging current, which is multiplied by the internal overpotentials within the cell. These overpotentials, including both ohmic and reaction-related components, increase as the current rises, leading to greater irreversible heat production. Consequently, at higher charging rates, the cell experiences more intense thermal buildup, which can elevate the risk of thermal instability if not properly managed. This emphasizes the importance of thermal modeling and management, particularly in high-rate charging applications where temperature control is critical for both performance and safety.

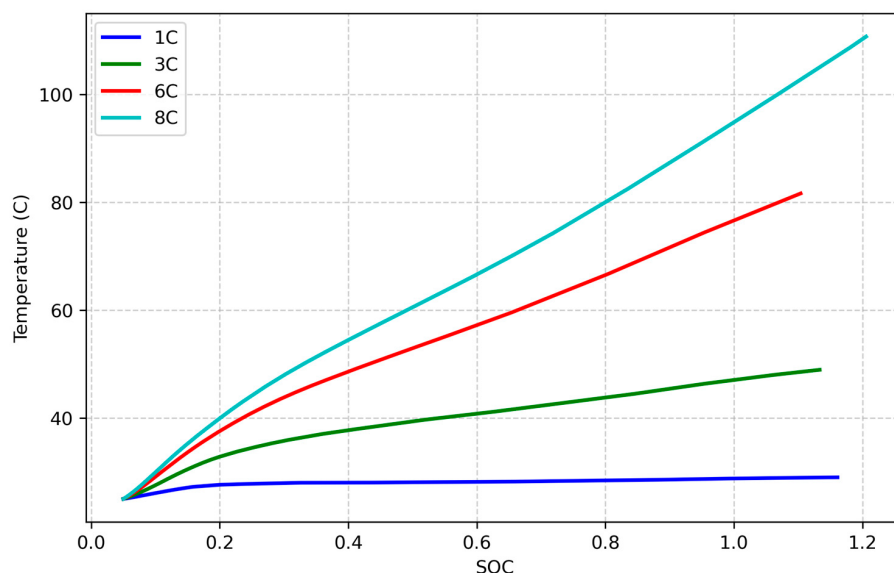


Figure 8. Temperature against SOC for four simulations with 1 Ah capacity, 10 mOhm internal resistance, and with charging rates of 1C, 3C, 6C, and 8C.

3.2. Effect of Internal Resistance on Thermal Runaway

To examine the impact of internal resistance on thermal behavior, simulations were conducted on NMC cells with identical capacities (5 Ah) and charging rates (3C) and different internal resistances (10, 20, 30, and 40 mΩ). Figure 9 shows the mean cell temperature (Average Cell Temperature) over time. The results reveal that a higher internal resistance correlates with increased cell temperature over the same time frame, leading to a higher likelihood of thermal runaway. This effect can be attributed to the additional heat generated by ohmic losses in the cell, and these findings agree with the results of Yoo et al. [45]. Since the internal resistance increase is often associated with battery aging, this means that aged cells are progressively more prone to thermal runaway events due to their increased thermal sensitivity, which is opposite of the study of Fleischhammer et al. [23] but in agreement with the study of Han et al. [46].

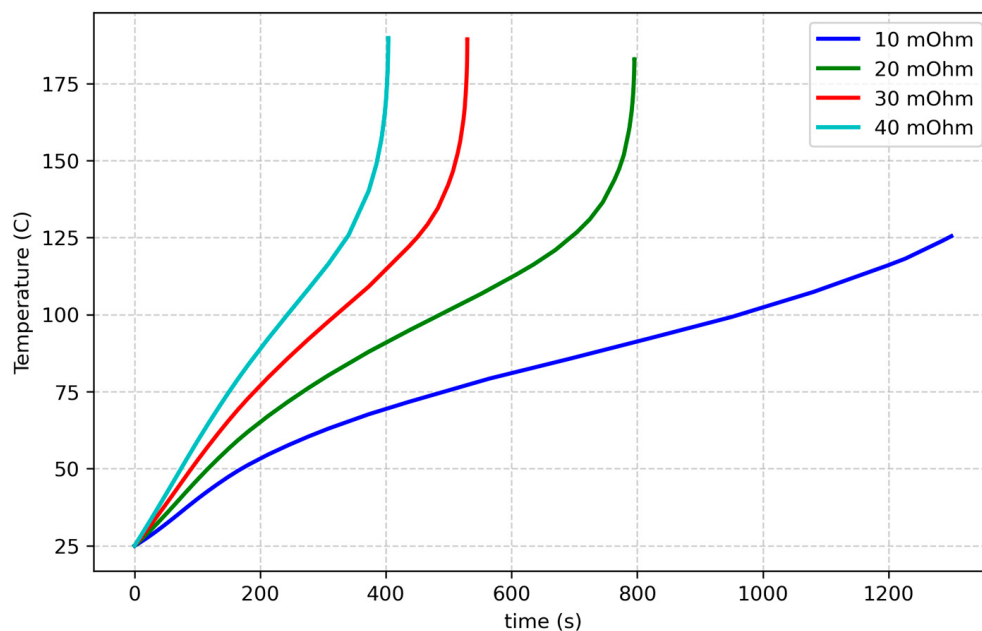


Figure 9. Temperature against time for simulations with 5 Ah capacity at 3C charging rate and with internal resistance of 10, 20, 30, and 40 mOhm.

3.3. Effect of Capacity on Thermal Runaway

The influence of cell capacity on thermal behavior was analyzed by comparing simulations with capacities of 1, 2, 3, and 5 Ah under a fixed internal resistance (30 mΩ) and a charging rate 3C. Figure 10 presents the temperature against time. The data indicate that higher capacity cells exhibit a more pronounced temperature rise with respect to lower capacity ones over a given SOC range, reflecting their greater energy content. Now, since a pronounced capacity fading is associated with cell aging, it derives that, from this point of view, the likelihood of a thermal runaway diminishes with age, along with reduced energy storage and associated thermal effects [47], due to the lower temperature reached. However, this does not necessarily diminish the likelihood of thermal runaway because, as discussed in the previous section, aged cells often exhibit increased internal resistance, leading to greater heat generation during operation and, thus, to a higher risk of thermal runaway. Therefore, despite their reduced capacity, aged cells may still be more prone to thermal runaway due to increased heat generation from higher internal resistance.

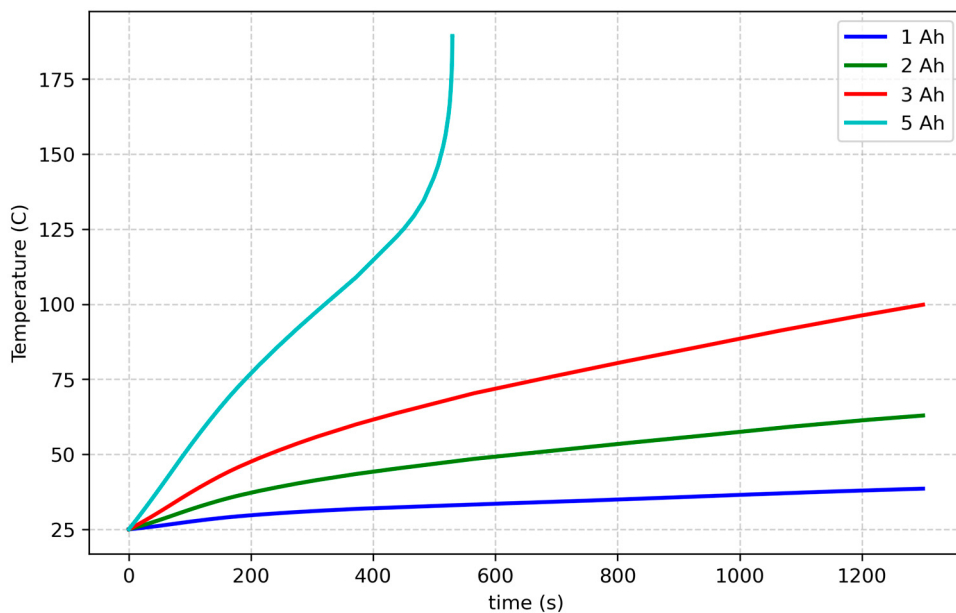


Figure 10. Temperature against time for simulations with 30 mOhm internal resistance and 3C charging rate and capacity of 1, 2, 3, and 5 Ah, in one single charge.

3.4. Combined Aging Effects

Based on the above results, the two primary aging effects, capacity fade and increased internal resistance, have opposing impacts on thermal behavior:

- An increased internal resistance exacerbates heat generation and thermal risks;
- Capacity fading mitigates thermal risk by reducing the total energy stored and released.

To fully understand these interactions and their implications for battery safety, statistical analyses are essential for quantifying their combined influence on the thermal behavior of aged cells.

3.5. ANOVA Analysis

After performing all the simulations, the mean temperature of the cell, its SOC, and the voltage of the cell against time were recorded. The necessary results obtained from the simulation for the ANOVA are shown in Table 4. This table presents data on battery thermal behavior across different test conditions, with a key focus on thermal runaway, temperature, and temperature change rate (dT/dt) at different states of charge (SOC). Run Order is the sequence in which the experiments were conducted, the thermal runaway column shows a binary indicator (0 = No thermal runaway, 1 = Thermal runaway occurred), and temperature and dT/dt at 10%, 50%, and 100% SOC reflect how the temperature and its rate of change evolve as the battery charges in a single charge phase. At 100% SOC, temperatures are often higher than at 50% and 10% SOC, which is expected as a fully charged battery generally has more stored energy to dissipate as heat. Starting from run 30, the first thermal runaway events are observed, where temperatures escalate drastically (e.g., Run 40: 169.5 °C at 100% SOC). In early runs (before thermal runaway events), dT/dt values remain low (mostly below 0.1 in different SOCs). However, once temperatures exceed certain thresholds, dT/dt rises steeply (e.g., Run 40: 2.374 at 100% SOC), indicating rapid heat generation and potential safety risks.

Table 4. Results obtained from full factorial design.

Run	TR	T at 10% SOC	dT/dt at 10% SOC	T at 50% SOC	dT/dt at 50% SOC	T at 100% SOC	dT/dt at 100% SOC	d ² T/dt ² at 100% SOC
1	0	25.5	0.003	26.3	0.000	26.6	0.000	-3.25×10^{-7}
2	0	25.5	0.003	26.5	0.000	26.9	0.000	-3.51×10^{-7}
3	0	25.6	0.003	26.7	0.000	27.1	0.000	-3.63×10^{-7}
4	0	25.6	0.004	26.9	0.000	27.4	0.000	-3.75×10^{-7}
5	0	26.1	0.006	28.1	0.000	28.8	0.000	-7.04×10^{-7}
6	0	26.3	0.007	28.9	0.000	29.7	0.000	-7.55×10^{-7}
7	0	26.5	0.008	29.7	0.001	30.7	0.001	-3.51×10^{-7}
8	0	26.6	0.009	30.5	0.001	31.6	0.001	-4.09×10^{-7}
9	0	26.7	0.010	30.2	0.000	31.4	0.001	-3.62×10^{-7}
10	0	27.2	0.012	32.1	0.001	33.6	0.001	-5.16×10^{-7}
11	0	27.6	0.014	33.9	0.001	35.7	0.001	-1.32×10^{-6}
12	0	28.0	0.016	35.7	0.002	37.9	0.001	-1.44×10^{-6}
13	0	28.4	0.019	36.4	0.001	38.3	0.001	-1.84×10^{-6}
14	0	29.6	0.025	41.7	0.002	44.4	0.001	-2.20×10^{-6}
15	0	30.8	0.031	47.0	0.003	50.5	0.001	-2.41×10^{-6}
16	0	32.0	0.037	52.3	0.005	56.5	0.002	-1.87×10^{-6}
17	0	26.1	0.022	31.0	0.005	34.3	0.006	-7.01×10^{-6}
18	0	26.3	0.025	32.0	0.006	35.9	0.007	-8.58×10^{-6}
19	0	26.4	0.027	33.1	0.007	37.5	0.007	-1.01×10^{-5}
20	0	26.6	0.029	34.1	0.009	39.1	0.008	-1.17×10^{-5}
21	0	27.5	0.049	39.4	0.014	47.1	0.013	-2.46×10^{-5}
22	0	28.2	0.059	43.6	0.019	53.6	0.015	-3.03×10^{-5}
23	0	28.8	0.069	47.8	0.025	60.2	0.018	-3.61×10^{-5}
24	0	29.4	0.079	52.0	0.031	66.8	0.021	-4.16×10^{-5}
25	0	29.3	0.081	49.9	0.025	63.5	0.022	-4.10×10^{-5}
26	0	30.7	0.103	59.4	0.039	78.5	0.028	-5.15×10^{-5}
27	0	32.0	0.126	69.0	0.052	94.0	0.038	-3.91×10^{-5}
28	0	33.4	0.148	78.6	0.066	113.5	0.068	0.0002
29	0	33.7	0.160	77.8	0.059	111.7	0.073	0.0001
30	1	37.5	0.222	105.6	0.104	—*	—*	—*
31	1	41.4	0.284	—*	—*	—*	—*	—*
32	1	45.2	0.346	—*	—*	—*	—*	—*
33	0	26.7	0.068	36.4	0.027	46.1	0.035	-1.84×10^{-5}
34	0	27.1	0.078	38.8	0.035	50.4	0.041	-3.02×10^{-5}
35	0	27.4	0.089	41.3	0.043	54.8	0.046	-4.18×10^{-5}
36	0	27.7	0.099	43.7	0.051	59.2	0.052	-5.34×10^{-5}
37	0	29.1	0.157	52.9	0.071	76.6	0.081	—0.0001
38	0	30.4	0.198	62.8	0.103	94.8	0.109	3.20×10^{-5}
39	1	31.6	0.239	72.7	0.135	115.5	0.166	0.0006
40	1	32.9	0.279	82.6	0.168	169.5	2.374	0.4273
41	1	32.1	0.267	74.8	0.134	123.3	0.253	0.0032
42	1	34.9	0.359	97.4	0.211	—*	—*	—*
43	1	37.8	0.451	122.3	0.347	—*	—*	—*
44	1	40.6	0.543	—*	—*	—*	—*	—*
45	1	40.0	0.548	152.3	1.220	—*	—*	—*
46	1	47.9	0.805	—*	—*	—*	—*	—*
47	1	55.8	1.062	—*	—*	—*	—*	—*

Table 4. Cont.

Run	TR	T at 10% SOC	dT/dt at 10% SOC	T at 50% SOC	dT/dt at 50% SOC	T at 100% SOC	dT/dt at 100% SOC	d ² T/dt ² at 100% SOC
48	1	63.7	1.318	- *	- *	- *	- *	- *
49	0	27.0	0.103	39.2	0.051	52.8	0.067	-5.32×10^{-5}
50	0	27.5	0.121	42.6	0.066	59.1	0.079	-8.28×10^{-5}
51	0	27.9	0.140	46.0	0.081	65.5	0.091	-0.0001
52	0	28.3	0.158	49.4	0.096	71.9	0.103	-0.0001
53	0	29.9	0.243	60.5	0.134	94.9	0.168	0.0001
54	1	31.6	0.316	74.3	0.196	124.9	0.294	0.003
55	1	33.3	0.390	88.1	0.258	- *	- *	- *
56	1	35.0	0.463	102.0	0.328	- *	- *	- *
57	1	33.7	0.420	89.3	0.255	- *	- *	- *
58	1	37.5	0.586	122.4	0.503	- *	- *	- *
59	1	41.3	0.751	- *	- *	- *	- *	- *
60	1	45.1	0.916	- *	- *	- *	- *	- *
61	1	43.7	0.888	- *	- *	- *	- *	- *
62	1	54.3	1.349	- *	- *	- *	- *	- *
63	1	64.9	1.811	- *	- *	- *	- *	- *
64	1	75.5	2.272	- *	- *	- *	- *	- *

* Indicates that the simulation could not proceed beyond this point due to the onset of thermal runaway.

In cells that did not experience thermal runaway (TR = 0), the temperature at 10% SOC generally remained below approximately 34 °C. In contrast, cells that underwent thermal runaway (TR = 1) typically exhibited temperatures above 35 °C at 10% SOC, with some values reaching over 40 °C. This suggests that a temperature exceeding around 35 °C at 10% SOC could serve as an early warning signal. For non-runaway cases, the rate of temperature rise at 10% SOC was usually below 0.16 °C/s. However, in cells that experienced thermal runaway, this rate exceeded approximately 0.22 °C/s. Thus, a dT/dt greater than about 0.2 °C/s at low SOC may indicate an increased risk. While non-thermal runaway cells typically maintained temperatures below around 80 °C at 50% SOC, cells prone to thermal runaway showed significantly higher temperatures, often exceeding 80 °C and, in some cases, reaching 100 °C or more. This marked increase reinforces the idea that a 50% SOC temperature above 80 °C might be a critical threshold. In cells that do not experience thermal runaway (TR = 0), the temperature at 100% SOC remains very low (typically below 40 °C). By contrast, in cases where thermal runaway occurs (TR = 1), the temperature at 100% SOC is substantially higher, often exceeding 100 °C and, in some cases, reaching values well above 150 °C. This dramatic increase indicates that once the runaway process is triggered, the battery temperature can escalate rapidly. For non-runaway cells, the first derivative of temperature (dT/dt) at 100% SOC is close to zero, reflecting a stable thermal state. However, in runaway cases, this rate becomes markedly elevated (e.g., over 2 °C/s in some instances), which suggests that the temperature is rising very rapidly (another clear sign of thermal instability). Similarly, the second derivative (d²T/dt²) in non-runaway scenarios remains extremely small (on the order of 10⁻⁵ °C/s²), indicating that the rate of temperature change is not accelerating significantly. In contrast, when thermal runaway occurs, the second derivative increases substantially (for example, values around 0.4273 °C/s²), demonstrating a rapidly accelerating temperature rise. In some instances, a battery may reach 100% SOC without immediately triggering a thermal runaway. However, if charging continues beyond this point, the risk of thermal runaway becomes highly probable, particularly when the temperature and its acceleration (the second derivative, d²T/dt²) are significantly elevated. In contrast, a non-thermal runaway case such as Run 28 shows much lower values at 100% SOC (113.5 °C with dT/dt of

0.068 °C/s and d^2T/dt^2 of 0.0002 °C/s²), suggesting a stable thermal condition. Thus, even if a cell does not immediately experience runaway at 100% SOC, continued charging under conditions where both temperature and its acceleration are high can quickly push the battery into an unstable, runaway state.

It is important to note that these values are based on the specific dataset and experimental conditions represented in Table 4, and further analysis across a broader range of conditions would be needed to generalize these thresholds.

Tables 5 and 6 present the analytical analysis and the regression model. The R^2 values provide insight into how well the model captures the variance in temperature and dT/dt at different states of charge (SOC). The highest R^2 (0.9621) for temperature at 10% SOC suggests that the model explains 96.2% of the variation in temperature at this charge level, demonstrating strong predictive accuracy. In contrast, the lowest R^2 (0.8205) for dT/dt at 50% SOC indicates that while the model still performs reasonably well, there is a greater degree of unexplained variability in the rate of temperature change at mid-range SOCs. Overall, the model effectively predicts temperature trends, though its accuracy in capturing dT/dt is comparatively lower.

Table 5. R^2 values of the regression models.

SOC	Temp (R^2)	dT/dt (R^2)
10%	96.21%	92.35%
50%	92.92%	82.05%
100%	93.51%	87.68%

Table 6. ANOVA and linear regression coefficients.

	SOC (%)	C_T ¹	P_T ²	C_d ³	P_d ⁴
Bias	10	24.4391	-	0.0761	-
	50	13.6308	-	-0.0655	-
	100	9.9273	-	-0.0408	-
Capacity	10	-1.8756	3.1474×10^{-17}	-0.0735	3.898×10^{-13}
	50	-0.6054	5.1716×10^{-26}	-0.0233	2.9529×10^{-24}
	100	-6.9376	1.49×10^{-22}	0.0389	0.04482
Current	10	-*	-*	-0.0496	1.1232×10^{-03}
	50	-1.9897	6.0723×10^{-04}	-0.0390	1.4285×10^{-07}
	100	-4.9313	2.098×10^{-10}	-*	-*
Resistance	10	-0.1520	9.0499×10^{-03}	-*	-*
	50	0.3777	1.0109×10^{-04}	0.0041	4.6553×10^{-08}
	100	0.8107	1.5789×10^{-04}	-*	-*
Capacity × Current	10	0.7209	1.7444×10^{-05}	0.0527	1.0182×10^{-02}
	50	4.4672	6.9643×10^{-12}	0.0373	5.3381×10^{-17}
	100	9.5669	9.0235×10^{-08}	-*	-*
Capacity × Resistance	10	0.1334	9.0783×10^{-03}	-*	-*
	50	0.0559	1.1416×10^{-05}	-0.0008	1.2349×10^{-15}
	100	0.05747	3.2543×10^{-04}	-*	-*
Current × Resistance	10	-*	-*	-*	-*
	50	-*	-*	-*	-*
	100	-*	-*	-*	-*

¹ Coefficient related to Temperature response; ² p -value related to Temperature response; ³ Coefficient related to Temperature derivative over time response; ⁴ p -value related to Temperature derivative over time response; * The p -value exceeds 0.05, and the parameter was not included in the final analysis.

The p -values for capacity are extremely low ($p < 0.05$, often much lower across different conditions), confirming that capacity has a strong and statistically significant impact on both temperature and dT/dt . Current also plays a significant role, with p -values < 0.05 in most cases, demonstrating its strong influence on thermal behavior. Internal resistance significantly influences temperature ($p < 0.01$ in most cases), and its coefficients are consistently positive, meaning that higher resistance leads to higher temperatures—a trend that aligns well with Joule heating principles. However, its effect on dT/dt is less consistent, suggesting that while internal resistance directly contributes to steady-state temperature rise, its impact on transient thermal behavior may be more complex and dependent on additional factors.

Notably, the coefficients for capacity and current are negative. However, the interaction between them is highly significant ($p < 0.05$ in all cases) and has a large coefficient, meaning their combined influence is critical in determining both temperature and dT/dt . This suggests that the relationship between capacity and current is not simply additive—rather, their combined influence plays a key role in determining overall thermal behavior. This highlights the importance of jointly managing capacity and current when optimizing thermal performance and ensuring battery safety rather than treating them as independent factors.

The interaction between capacity and internal resistance is also significant, though its effect size is smaller, indicating that while capacity influences resistance-driven heating, its effect is secondary compared to direct resistance contributions. Interestingly, the interaction between current and internal resistance shows no significant impact, suggesting that resistance-related heating is largely independent of current within the tested operating conditions. This finding implies that internal resistance effects may be more static and intrinsic to the cell's electrochemical characteristics rather than dynamically varying with current load.

Overall, these findings highlight the complex interplay between capacity, current, and internal resistance in shaping battery thermal behavior. The insights gained from this analysis can aid in the development of more effective thermal management strategies, improve battery performance predictions, and enhance safety measures in high-energy applications.

3.6. Internal Resistance Threshold

Table 7 presents the computed values corresponding to Equation (21), which are essential for determining the internal resistance threshold. Additionally, Figure 11 illustrates the confusion matrix for the classification task performed using the logistic regression model on the test set. The model demonstrates strong predictive performance, achieving an accuracy of 95%, indicating its reliability in distinguishing between thermal runaway and non-thermal runaway cases.

Table 7. Parameters for logistic regression model.

Parameters	Values
b_0	-0.3963
b_1	-0.0491
b_2	0.1300
b_3	0.2386

The confusion matrix represents the classification performance of the model, where rows indicate actual values and columns indicate predicted values. The top-left value (8) represents true positive (TP), meaning the model correctly predicted 8 cases where thermal runaway occurred. The top-right value (0) represents false positives (FP), indicating no incorrect predictions of thermal runaway when it did not actually happen. The bottom-left

value (1) represents false negatives (FN), meaning one case of not thermal runaway classified as thermal runaway. Lastly, the bottom-right value (11) represents true negatives (TN), where the model correctly identified 11 instances of not thermal runaway. From the figure, it can be concluded that the model performs well in terms of avoiding risks, i.e., it never ensures a lack of a thermal runaway when it actually occurs. By leveraging the proposed logistic regression model, the internal resistance threshold can be determined by fixing the charging current, capacity of the cell, and probability of thermal runaway occurrence. This approach allows for precise identification of the critical resistance value beyond which the likelihood of thermal runaway significantly increases. The results obtained from this analysis can be instrumental in enhancing battery safety, enabling proactive measures such as real-time monitoring, thermal management, and early fault detection.

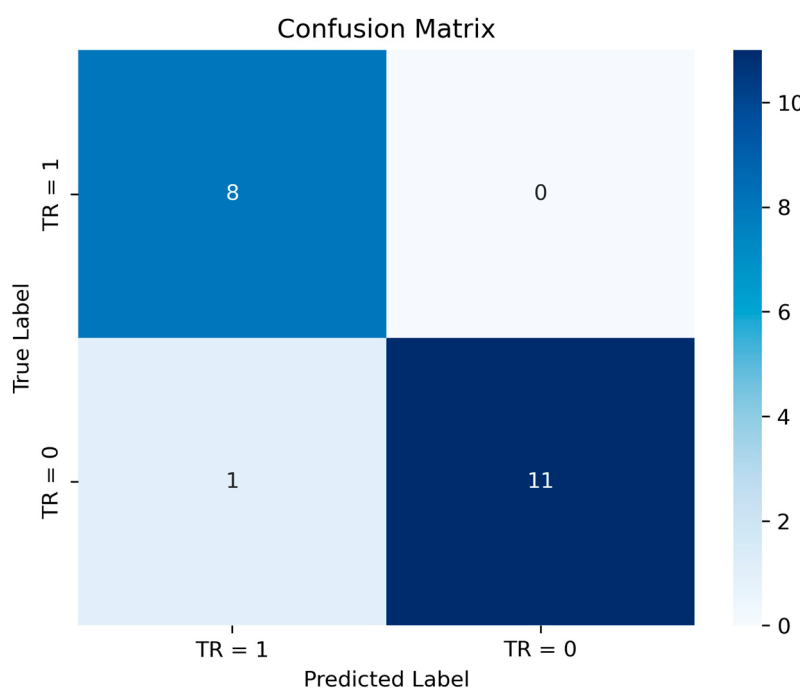


Figure 11. Confusion matrix for classification task.

4. Conclusions

One of the most critical safety hazards connected with lithium-ion batteries is thermal runaway. While mechanical abuse is often unpredictable, other types of failures are frequently caused by system faults. Battery aging is a key contributor to such failures, as it reduces thermal stability and decreases a cell's ability to tolerate faults.

To investigate how aging impacts the thermal sensitivity of lithium-ion cells, this study focused on three key parameters: capacity, internal resistance, and current. A thermal model was developed to incorporate internal resistance as a proxy for aging and thermal runaway side reactions.

The results demonstrate that the interaction between capacity, internal resistance, and charging rate significantly influences thermal behavior and the likelihood of thermal runaway. At low charging rates (1C), cells with higher internal resistance exhibit increased temperature rise, particularly in high-capacity cells. In contrast, low-capacity cells show minimal temperature deviations due to their lower energy density. As the charging rate increases, heat generation intensifies, with several high-capacity simulations exceeding the critical 90 °C threshold, a known precursor to thermal runaway. Notably, cells with both

high capacity and high internal resistance experience the most severe temperature spikes, indicating a compounded effect of Joule heating.

A statistical analysis confirmed that capacity, current, and internal resistance are major determinants of battery thermal behavior. Capacity has a significant impact on temperature rise and dT/dt , while current plays a crucial role in heat generation. Internal resistance is strongly correlated with temperature increase due to Joule heating, though its effect on dT/dt is less predictable. A key finding is that the interaction between capacity and current is highly significant, meaning their combined influence is nonlinear. In contrast, the interaction between current and internal resistance was found to be negligible, suggesting that resistance-related heating remains relatively independent of applied current within the tested range. These insights reinforce the importance of an integrated thermal management strategy, particularly in aged batteries where resistance and capacity degrade at different rates.

A machine learning approach was also adopted to classify thermal runaway events based on battery conditions. This approach holds promise for real-time battery monitoring and early failure detection and offers potential applications in BMS algorithms for enhancing battery safety and longevity.

However, battery aging is a complex phenomenon that, besides the internal resistance, also affects other parameters like active material composition, thermal conductivity, and heat generation. Therefore, additional work is required to integrate these aging mechanisms into a more comprehensive model for a more accurate representation of aged battery behavior. Doing so will improve predictive capabilities, enhance thermal management strategies, and ultimately ensure safer battery operation in real-world applications.

Author Contributions: Conceptualization, R.B.; Data curation, M.T.; Funding acquisition, R.B.; Investigation, M.T.; Methodology, M.T. and R.B.; Software, M.T.; Supervision, R.B.; Validation, M.T.; Writing—original draft, M.T.; Writing—review and editing, R.B. All authors have read and agreed to the published version of the manuscript.

Funding: The results of this work have been obtained with the financial support of the National Recovery and Resilience Plan (PNRR), Mission 4 Component 2 Investment 1.3, funded by the European Union—NextGenerationEU, Spoke 6 “Energy Storage” of the Extended Partnership (PE2) NEST—Network 4 Energy Sustainable Transition.

Data Availability Statement: The raw data supporting the conclusions of this article will be made available by the authors on request.

Conflicts of Interest: The authors declare no conflicts of interest.

Abbreviations

The following abbreviations are used in this manuscript:

ANOVA	analysis of variance
ARC	Accelerating Rate Calorimetry
DOD	depth of discharge
DOE	design of experiments
EIS	Electrochemical Impedance Spectroscopy
EV	electric vehicle
HTC	heat transfer coefficient
HTR	Heat–Temperature–Reaction
P2D	pseudo-2D
SEI	solid electrolyte interface
SP	single-particle
SOC	state of charge

TR thermal runaway

References

- Wang, J.; Azam, W. Natural resource scarcity, fossil fuel energy consumption, and total greenhouse gas emissions in top emitting countries. *Geosci. Front.* **2024**, *15*, 101757. [[CrossRef](#)]
- Wen, J.; Yu, Y.; Chen, C. A review on lithium-ion batteries safety issues: Existing problems and possible solutions. *Mater. Express* **2012**, *2*, 197–212. [[CrossRef](#)]
- Chen, S.C.; Wan, C.C.; Wang, Y.Y. Thermal analysis of lithium-ion batteries. *J. Power Sources* **2005**, *140*, 111–124. [[CrossRef](#)]
- Feng, X.; Ouyang, M.; Liu, X.; Lu, L.; Xia, Y.; He, X. Thermal runaway mechanism of lithium ion battery for electric vehicles: A review. *Energy Storage Mater.* **2018**, *10*, 246–267. [[CrossRef](#)]
- Menale, C.; D’Annibale, F.; Mazzarotta, B.; Bubbico, R. Thermal management of lithium-ion batteries: An experimental investigation. *Energy* **2019**, *182*, 57–71. [[CrossRef](#)]
- Hendricks, C.; Williard, N.; Mathew, S.; Pecht, M. A failure modes, mechanisms, and effects analysis (FMMEA) of lithium-ion batteries. *J. Power Sources* **2015**, *297*, 113–120. [[CrossRef](#)]
- Bubbico, R.; Greco, V.; Menale, C. Hazardous scenarios identification for Li-ion secondary batteries. *Saf. Sci.* **2018**, *108*, 72–88. [[CrossRef](#)]
- Wang, Q.; Ping, P.; Zhao, X.; Chub, G.; Sun, J.; Chen, C. Thermal runaway caused fire and explosion of lithium ion battery. *J. Power Sources* **2012**, *208*, 210–224. [[CrossRef](#)]
- Kim, G.H.; Pesaran, A.; Spotnitz, R. A three-dimensional thermal abuse model for lithium-ion cells. *J. Power Sources* **2007**, *170*, 476–489. [[CrossRef](#)]
- Doyle, M.; Fuller, T.F.; Newman, J. Modeling of galvanostatic charge and discharge of the lithium/polymer/insertion cell. *J. Electrochem. Soc.* **1993**, *140*, 1526. [[CrossRef](#)]
- Doyle, M.; Newman, J.; Gozdz, A.S.; Schmutz, C.N.; Tarascon, J.M. Comparison of modeling predictions with experimental data from plastic lithium ion cells. *J. Electrochem. Soc.* **1996**, *143*, 1890. [[CrossRef](#)]
- Guo, M.; Sikha, G.; White, R.E. Single-particle model for a lithium-ion cell: Thermal behavior. *J. Electrochem. Soc.* **2010**, *158*, A122. [[CrossRef](#)]
- Wu, L.; Liu, K.; Liu, J.; Pang, H. Evaluating the heat generation characteristics of cylindrical lithium-ion battery considering the discharge rates and N/P ratio. *J. Energy Storage* **2023**, *64*, 107182. [[CrossRef](#)]
- Hatchard, T.D.; MacNeil, D.D.; Basu, A.; Dahn, J.R. Thermal model of cylindrical and prismatic lithium-ion cells. *J. Electrochem. Soc.* **2001**, *148*, A755. [[CrossRef](#)]
- Talele, V.; Morali, U.; Patil, M.S.; Panchal, S.; Fraser, R.; Fowler, M.; Thorat, P.; Gokhale, Y.P. Computational modelling and statistical evaluation of thermal runaway safety regime response on lithium-ion battery with different cathodic chemistry and varying ambient condition. *Int. Commun. Heat Mass Transf.* **2023**, *146*, 106907. [[CrossRef](#)]
- Azuaje-Berbecí, B.J.; Ertan, H.B. A model for the prediction of thermal runaway in lithium-ion batteries. *J. Energy Storage* **2024**, *90*, 111831. [[CrossRef](#)]
- Ozdemir, T.; Ekici, O.; Koksal, M. Numerical and experimental investigation of the electrical and thermal behaviors of the Li-ion batteries under normal and abuse operating conditions. *J. Energy Storage* **2024**, *77*, 109880. [[CrossRef](#)]
- Wu, S.; Wang, C.; Luan, W.; Zhang, Y.; Chen, Y.; Chen, H. Thermal runaway behaviors of Li-ion batteries after low temperature aging: Experimental study and predictive modeling. *J. Energy Storage* **2023**, *66*, 107451. [[CrossRef](#)]
- García, A.; Monsalve-Serrano, J.; de Vargas Lewiski, F.; Golke, D. Characterization of pristine and aged NMC lithium-ion battery thermal runaway using ARC experiments coupled with optical techniques. *Appl. Therm. Eng.* **2024**, *257*, 124244. [[CrossRef](#)]
- Wang, Y.; Xiang, H.; Soo, Y.Y.; Fan, X. Aging mechanisms, prognostics and management for lithium-ion batteries: Recent advances. *Renew. Sustain. Energy Rev.* **2025**, *207*, 114915. [[CrossRef](#)]
- Galatro, D.; Al-Zareer, M.; Da Silva, C.; Romero, D.; Amon, C. Thermal behavior of lithium-ion batteries: Aging, heat generation, thermal management and failure. *Front. Heat Mass Transf. (FHMT)* **2020**, *27*, 14. [[CrossRef](#)]
- Birk, C.R.; Roberts, M.R.; McTurk, E.; Bruce, P.G.; Howey, D.A. Degradation diagnostics for lithium ion cells. *J. Power Sources* **2017**, *341*, 373–386. [[CrossRef](#)]
- Fleischhammer, M.; Waldmann, T.; Bisile, G.; Hogg, B.I.; Wohlfahrt-Mehrens, M. Interaction of cyclic ageing at high-rate and low temperatures and safety in lithium-ion batteries. *J. Power Sources* **2015**, *274*, 432–439. [[CrossRef](#)]
- Röder, P.; Stiaszny, B.; Ziegler, J.C.; Baba, N.; Lagaly, P.; Wiemhöfer, H.D. The impact of calendar aging on the thermal stability of a LiMn₂O₄–Li (Ni_{1/3}Mn_{1/3}Co_{1/3})O₂/graphite lithium-ion cell. *J. Power Sources* **2014**, *268*, 315–325. [[CrossRef](#)]
- Guo, Y.; Cai, J.; Liao, Y.; Hu, J.; Zhou, X. Insight into fast charging/discharging aging mechanism and degradation-safety analytics of 18650 lithium-ion batteries. *J. Energy Storage* **2023**, *72*, 108331. [[CrossRef](#)]
- Zhang, G.; Wei, X.; Chen, S.; Wei, G.; Zhu, J.; Wang, X.; Han, G.; Dai, H. Research on the impact of high-temperature aging on the thermal safety of lithium-ion batteries. *J. Energy Chem.* **2023**, *87*, 378–389. [[CrossRef](#)]

27. Zhang, G.; Shen, W.; Wei, X. Lithium-ion battery thermal safety evolution during high-temperature nonlinear aging. *Fuel* **2024**, *362*, 130845. [[CrossRef](#)]
28. Abada, S.; Petit, M.; Lecocq, A.; Marlair, G.; Sauvant-Moynot, V.; Huet, F. Combined experimental and modeling approaches of the thermal runaway of fresh and aged lithium-ion batteries. *J. Power Sources* **2018**, *399*, 264–273. [[CrossRef](#)]
29. Grandjacques, M.; Kuntz, P.; Azaïs, P.; Genies, S.; Raccourt, O. Thermal runaway modelling of Li-ion cells at various states of ageing with a semi-empirical model based on a kinetic equation. *Batteries* **2021**, *7*, 68. [[CrossRef](#)]
30. Zhao, L.; Zheng, M.; Zhang, J.; Liu, H.; Li, W.; Chen, M. Numerical modeling of thermal runaway for low temperature cycling lithium-ion batteries. *J. Energy Storage* **2023**, *63*, 107053. [[CrossRef](#)]
31. Pastor, J.V.; García, A.; Monsalve-Serrano, J.; Golke, D. Analysis of the aging effects on the thermal runaway characteristics of Lithium-Ion cells through stepwise reactions. *Appl. Therm. Eng.* **2023**, *230*, 120685. [[CrossRef](#)]
32. Kabra, V.; Karmakar, A.; Vishnugopi, B.S.; Mukherjee, P.P. Quantifying the effect of degradation modes on Li-ion battery thermal instability and safety. *Energy Storage Mater.* **2025**, *74*, 103878. [[CrossRef](#)]
33. NASA Dataset. Available online: <https://phm-datasets.s3.amazonaws.com/NASA/5.+Battery+Data+Set.zip> (accessed on 8 October 2024).
34. Ekström, H.; Fridholm, B.; Lindbergh, G. Comparison of lumped diffusion models for voltage prediction of a lithium-ion battery cell during dynamic loads. *J. Power Sources* **2018**, *402*, 296–300. [[CrossRef](#)]
35. Cai, L.; White, R.E. Mathematical modeling of a lithium ion battery with thermal effects in COMSOL Inc. Multiphysics (MP) software. *J. Power Sources* **2011**, *196*, 5985–5989. [[CrossRef](#)]
36. Kumaresan, K.; Sikha, G.; White, R.E. Thermal model for a Li-ion cell. *J. Electrochem. Soc.* **2007**, *155*, A164. [[CrossRef](#)]
37. Chen, S.C.; Wang, Y.Y.; Wan, C.C. Thermal analysis of spirally wound lithium batteries. *J. Electrochem. Soc.* **2006**, *153*, A637. [[CrossRef](#)]
38. Cianciullo, M.; Vilardi, G.; Mazzarotta, B.; Bubbico, R. Simulation of the Thermal Runaway Onset in Li-Ion Cells—Influence of Cathode Materials and Operating Conditions. *Energies* **2022**, *15*, 4169. [[CrossRef](#)]
39. Peng, P.; Jiang, F. Thermal safety of lithium-ion batteries with various cathode materials: A numerical study. *Int. J. Heat Mass Transf.* **2016**, *103*, 1008–1016. [[CrossRef](#)]
40. Tran, M.K.; DaCosta, A.; Mevawalla, A.; Panchal, S.; Fowler, M. Comparative study of equivalent circuit models performance in four common lithium-ion batteries: LFP, NMC, LMO, NCA. *Batteries* **2021**, *7*, 51. [[CrossRef](#)]
41. Mei, W.; Zhang, L.; Sun, J.; Wang, Q. Experimental and numerical methods to investigate the overcharge caused lithium plating for lithium ion battery. *Energy Storage Mater.* **2020**, *32*, 91–104. [[CrossRef](#)]
42. Dong, T.; Peng, P.; Jiang, F. Numerical modeling and analysis of the thermal behavior of NCM lithium-ion batteries subjected to very high C-rate discharge/charge operations. *Int. J. Heat Mass Transf.* **2018**, *117*, 261–272. [[CrossRef](#)]
43. Liu, Z.; Guo, X.; Meng, N.; Yu, Z.; Yang, H. Study of thermal runaway and the combustion behavior of lithium-ion batteries overcharged with high current rates. *Thermochim. Acta* **2022**, *715*, 179276. [[CrossRef](#)]
44. Hellwig, C.; Sörgel, S.; Bessler, W.G. A multi-scale electrochemical and thermal model of a LiFePO₄ battery. *Ecs Trans.* **2011**, *35*, 215. [[CrossRef](#)]
45. Yoo, K.; Kim, J. Thermal behavior of full-scale battery pack based on comprehensive heat-generation model. *J. Power Sources* **2019**, *433*, 226715. [[CrossRef](#)]
46. Han, Z.; Zhao, L.; Zhao, J.; Xu, G.; Liu, H.; Chen, M. An experimental study on the thermal runaway propagation of cycling aged lithium-ion battery modules. *Fire* **2024**, *7*, 119. [[CrossRef](#)]
47. Wei, N.; Zhang, F.; Zhang, W.; Li, X. Comparative study on the thermal runaway characteristics of Li (Ni_xCoyMn_z)O₂ batteries. *Heliyon* **2024**, *10*, e31203. [[CrossRef](#)]

Disclaimer/Publisher’s Note: The statements, opinions and data contained in all publications are solely those of the individual author(s) and contributor(s) and not of MDPI and/or the editor(s). MDPI and/or the editor(s) disclaim responsibility for any injury to people or property resulting from any ideas, methods, instructions or products referred to in the content.